5-17-2023

Discovery of Nanoscale Electric Field-Induced Phase Transitions in ZrO_2

Patrick D. Lomenzo

Liam Collins

Richard Ganser

Bohan Xu

Roberto Guido

See next page for additional authors

Authors

Patrick D. Lomenzo, Liam Collins, Richard Ganser, Bohan Xu, Roberto Guido, Alexei Gruverman, Alfred Kersch, Thomas Mikolajick, and Mikolajick Schroeder

ADVANCED FUNCTIONAL MATERIALS
www.afm-journal.de

Discovery of Nanoscale Electric Field-Induced Phase Transitions in ZrO_2

Patrick D. Lomenzo, Liam Collins, Richard Ganser, Bohan Xu, Roberto Guido, Alexei Gruverman, Alfred Kersch, Thomas Mikolajick,* and Uwe Schroeder*

The emergence of ferroelectric and antiferroelectric properties in the semiconductor industry's most prominent high-k dielectrics, HfO_2 and ZrO_2, is leading to technology developments unanticipated a decade ago. Yet the failure to clearly distinguish ferroelectric from antiferroelectric behavior is impeding progress. Band-excitation piezoresponse force microscopy and molecular dynamics are used to elucidate the nanoscale electric field-induced phase transitions present in ZrO_2-based antiferroelectrics. Antiferroelectric ZrO_2 is clearly distinguished from a closely resembling pinched La-doped HfO_2 ferroelectric. Crystalline grains in the range of 3 – 20 nm are imaged independently undergoing reversible electric field induced phase transitions. The electrically accessible nanoscale phase transitions discovered in this study open up an unprecedented paradigm for the development of new nanoelectronic devices.

1. Introduction

As the means by which states of matter and energy change forms, phase transitions emerge at the boundaries of human knowledge from cosmological models of the early universe to quantum physics.[1–3] Hidden within all modern computer chips is a dielectric bearing an enigmatic phase transition that has eluded direct observation, yet could lead to far-reaching transformations in computing, transducing, and energy technologies. ZrO_2, like its fluorite-structured sister oxide HfO_2, has shown ferroelectric (FE) and antiferroelectric (AFE) properties in recent years that are stimulating a flurry of activity in the development of a new generation of memories, steep slope transistors, high energy storage capacitors, and transducers.[4–8]

There is a growing number of remarkable demonstrations of new devices and technologies leveraging antiferroelectric HfO_2 and ZrO_2 at the laboratory and chip-scale.[9–11] However, the operating physics of AFE behavior in these high-k dielectrics is still not well understood, unlike the ferroelectric behavior in HfO_2 and ZrO_2. Scientists have not been able to provide direct evidence to rule out competing theories of AFE behavior, largely due to the similarities in many experimental features of fluorite-structured FEs and AFEs. This confusion is impeding state-of-the-art advancements in modern digital and emerging computing technologies, such as neuromorphic computing and artificial intelligence.[12,13]

Ferroelectricity in these fluorite-structured dielectrics originates from the polar orthorhombic (o) $Pca2_1$ phase.[14,15] Double hysteresis loops, on the other hand, have been one of the primary signatures of AFE in ZrO_2 and frequently attributed to reversible electric field-induced phase transitions from the nonpolar tetragonal (t) $P4_2/nmc$ phase to the polar o-phase.[15–17] Density functional theory (DFT) calculations and phenomenological Landau-based models have shown that the small energy difference between the ground states of the t- and o-phases in HfO_2 and ZrO_2 can be reversibly changed by electric fields.[15,18] By applying a strong enough electric field, the energy minimum of the o-phase is lowered until it becomes the stable ground state of the material system and a tetragonal to orthorhombic phase transition occurs. Conversely, removing the electric field reconfigures the energy landscape making the nonpolar t-phase the stable ground state, causing a reverse orthorhombic to tetragonal phase transition.

Such reversible electric field-induced phase transitions explain the nonlinear polarization-voltage characteristics so often found in the double-hysteresis loop behavior of ZrO_2.[19–25] The first-

P. D. Lomenzo, B. Xu, R. Guido, T. Mikolajick, U. Schroeder
NaMLab gGmbH
Technische Universität Dresden
Noethnitzer Str. 64a, 01187 Dresden, Germany
E-mail: Patrick.Lomenzo@namlab.com;
thomas.mikolajick@namlab.com

L. Collins
Center for Nanophase Materials Sciences
Oak Ridge National Laboratory
Oak Ridge, TN 37831, USA

R. Ganser, A. Kersch
Department of Applied Sciences and Mechatronics
Munich University of Applied Sciences
Lothstr. 34, 80335 Munich, Germany

A. Gruverman
Department of Physics and Astronomy
University of Nebraska-Lincoln Lincoln
lincoln, NE 68588, USA

The ORCID identification number(s) for the author(s) of this article can be found under https://doi.org/10.1002/adfm.202303636

DOI: 10.1002/adfm.202303636

order nature of the phase transition is predicted by Landau theory and supported by experimental observations of temperature-induced phase transitions of the ferroelectric o-phase to the nonpolar t-phase.[18,26,27] The electric field-induced phase transitions generating AFE behavior, however, have remained hidden from view despite theoretical and supporting experimental evidence. Direct physical observations are needed for greater exploitation of this nonlinear phenomenon to pave the way for next-generation steep-slope transistors, antiferroelectric-based memories, supercapacitors, neuromorphic devices, and transducers.[9,13,19–22,28]

The ability to probe the piezoelectric behavior of FEs and AFEs at the microscopic scale makes piezoresponse force microscopy (PFM) a suitable technique to investigate the physics of AFE device behavior more clearly. PFM has been previously applied to distinguish the nonlinear piezoelectric response of AFE ZrO_2 with respect to FE La-doped HfO_2.[22] Although the nonlinear piezoelectric response during PFM hysteresis excitation experimentally indicated the active role of electric field-induced phase transitions, PFM imaging of the AFE capacitor surface conspicuously revealed little detail.[22]

By using band excitation piezoresponse force microscopy (BE-PFM),[29] we have discovered direct evidence of an electric field-induced phase transition operating at the nanoscale in ZrO_2-based antiferroelectrics. The significance of this discovery not only gives us an unprecedented physical view of antiferroelectricity in fluorite-structured materials, but even allows us to unambiguously distinguish AFE from its closely resembling FE counterparts. Microscopic insight is furthermore provided by comparing ZrO_2 and $Zr_{0.87}Hf_{0.13}O_2$, showing that Hf-doping enhances the piezoelectric response and lowers the phase-transition fields due to the material's closer proximity to the tetragonal and orthorhombic morphotropic phase boundary.

2. Distinguishing AFE ZrO_2 from Pinched FE La-Doped HfO_2

FE doped HfO_2, such as La-doped HfO_2, often exhibits an AFE-like characteristic marked by a pinched polarization-electric field (P-E) hysteresis loop[30,31] that resembles AFE ZrO_2, as seen in **Figure 1**a. La-doped HfO_2 has a notably pinched P-E hysteresis loop and four switching currents as shown in Figure 1b, bearing similar overall features as ZrO_2 during dynamic hysteresis measurements. Despite having a pinched P-E hysteresis loop, La-doped HfO_2 still exhibits a nonzero remanent polarization, in contrast to ZrO_2. Moreover, ZrO_2 switching currents are found in all four quadrants, while La-doped HfO_2 has four switching peaks that are only located in two quadrants. The location of the four switching peaks in only two quadrants is frequently associated with internally biased or pinned FE domains, whereas four switching peaks in four quadrants are characteristic of AFE behavior.[32]

Despite the differences, the similarities between AFE and pinched FE hysteresis loops have led to theories that challenge the authenticity of AFE in fluorites-structured materials. There have been suggestions that AFE behavior may be the result of charged ionic defects and pinned ferroelectric or ferroelastic domains, rather than reversible electric field-induced phase transitions.[33–35] The apparent device-terminal similarities and the fluid transformation of pinched to square FE hysteresis

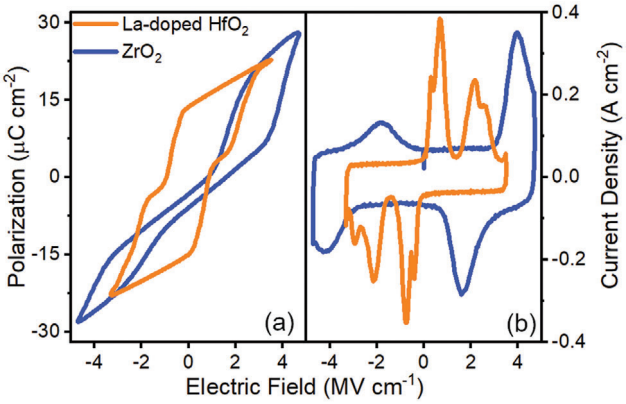

Figure 1. a) Polarization versus electric field and b) current density versus electric field dynamic hysteresis measurements of ZrO_2 and La-doped HfO_2. Both films share similar shaped hysteresis curves with characteristic pinching in polarization near low fields and four switching current peaks.

loops with field cycling, commonly called "wake-up", in fluorite-structured FEs further add to the confusion.[33–35]

The challenge of distinguishing between FE and AFE in fluorite-structured materials, which is critical for advancing technology, stems from not one but several experimental limitations: i) The FE polar orthorhombic (o) $Pca2_1$ phase is structurally similar to the nonpolar tetragonal (t) $P4_2/nmc$ phase, obfuscating clear identification of the phases in thin films by grazing incidence x-ray diffraction (GIXRD).[36] ii) AFE behavior is widely attributed to a reversible electric field-induced tetragonal to polar orthorhombic phase transition, but it has been challenging to obtain unambiguous structural identification of the phase transition under applied fields.[36,37] iii) An irreversible electric-field driven tetragonal to orthorhombic phase transition has been observed and may cause "wake-up".[38] iv) FE domains cannot be directly observed from electrical device measurements, but must be inferred from behavioral models at the device terminals.[33,39]

To overcome these experimental limitations, BE-PFM can be utilized as a powerful technique to directly image FE domains at the microscopic scale with enhanced sensitivity.[40] **Figure 2** presents BE-PFM images of La-doped HfO_2 and ZrO_2, which clearly shows the presence of FE domains in La-doped HfO_2. In contrast, no discernible features are observed in ZrO_2. The lack of FE domains in ZrO_2 provides conclusive evidence that the double hysteresis loop of ZrO_2 does not originate from FE domain pinning,[41] despite sharing qualitatively similar "pinched" hysteresis characteristics with La-doped HfO_2. This result firmly rules out any involvement of FE domains in the pinched hysteresis loop characteristics originating from AFE in ZrO_2.

3. Piezoelectric Response of Electric Field-Induced Phase Transition in ZrO_2

To further investigate AFE films using BE-PFM, we conducted hysteresis spectroscopy measurements on ZrO_2 and $Zr_{0.87}Hf_{0.13}O_2$. Hf-doping pushes ZrO_2 closer to the t- and o-morphotropic phase boundary (MPB) which improves the visibility of the tetragonal to polar orthorhombic field-induced phase

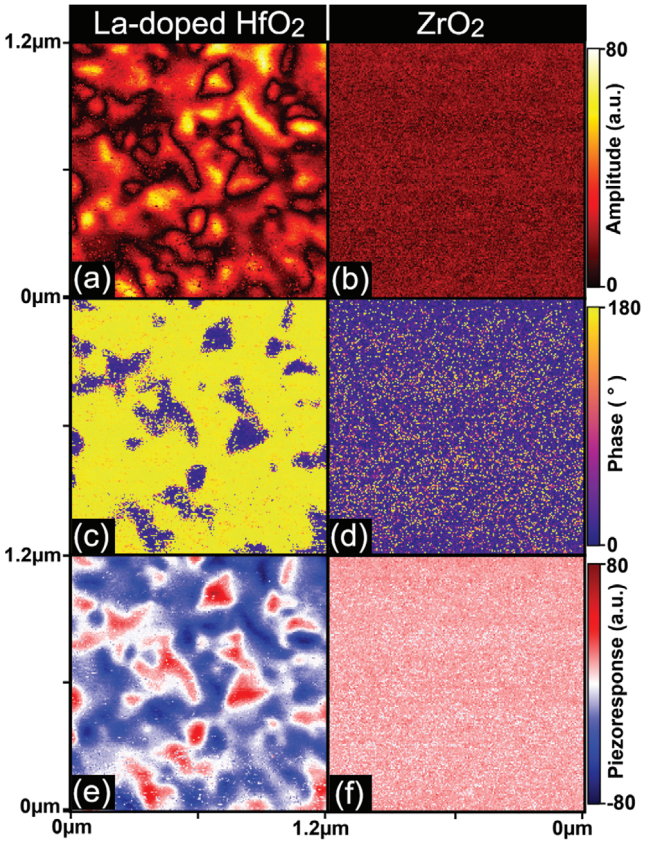

Figure 2. BE-PFM images on top of a La-doped HfO_2 and a ZrO_2 capacitor. a,b) Amplitude, c,d) phase, and e,f) piezoresponse showing ferroelectric domains are present in La-doped HfO_2, but such features are not resolvable for ZrO_2.

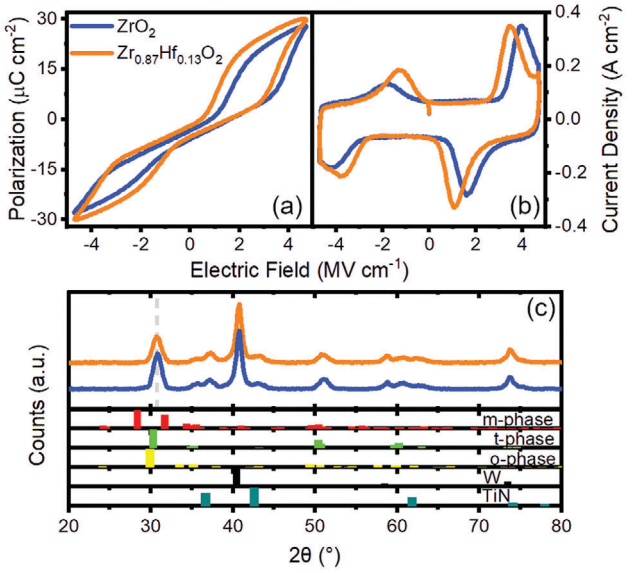

Figure 3. a) Polarization versus electric field, b) current density versus electric field, and c) GIXRD counts versus 2θ of ZrO_2 and $Zr_{0.87}Hf_{0.13}O_2$. The double hysteresis loop behavior and diffraction pattern are consistent with a reversible tetragonal to orthorhombic field-induced phase transition.

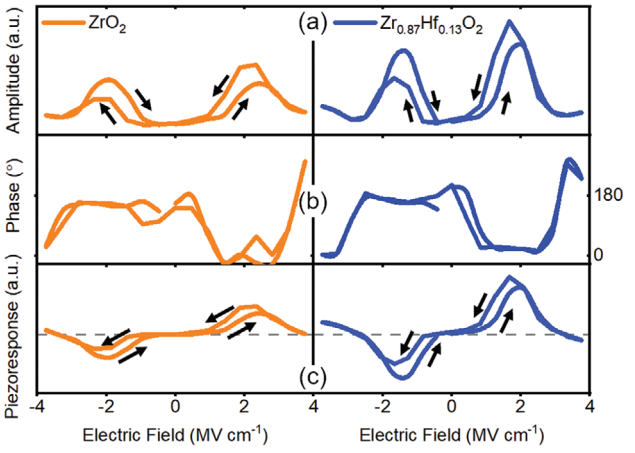

Figure 4. PFM mean a) amplitude-, b) phase-, and c) piezoresponse versus electric field for ZrO_2 and $Zr_{0.87}Hf_{0.13}O_2$. The mean is calculated only from pixels undergoing the phase transitions identified by the quad-peaked amplitude response. The phase transition electric fields are lower while the amplitude and piezoresponse are higher in magnitude in Hf-doped ZrO_2.

transition by reducing the phase transition field.[12] The choice of these two ZrO_2-based compositions is motivated by the goal to approach the MPB without causing electric field-induced irreversible phase transitions ("wake-up"). Polarization versus electric field characteristics of ZrO_2 and $Zr_{0.87}Hf_{0.13}O_2$ show that both films exhibit double hysteresis loops, as seen in **Figure 3**a. The magnitude of switching charge is enhanced and the phase transition fields are smaller in $Zr_{0.87}Hf_{0.13}O_2$ compared to ZrO_2, confirming Hf-doping causes the films to be in closer proximity to the t/o-phase MPB. The non-switching regions of the current density versus electric field curve shown in Figure 3b indicate that the relative permittivity is quite similar between the two AFE films. The asymmetry in the magnitudes of the switching charge associated with the field-induced phase transition polarity likely originates from the relatively more oxidized bottom TiN electrode compared to the top TiN electrode, as has been reported by others.[42–44]

Grazing incidence x-ray diffraction (GIXRD) shows that the two ZrO_2-based films are consistent with the tetragonal phase with the major $(011)_t$ diffraction peak showing up at ≈30°, as seen in Figure 3c. Due to the polycrystalline nature and thinness of the 8 nm ZrO_2-based films, it is very difficult to unambiguously distinguish the tetragonal and orthorhombic phase with certainty.[45] The low-k monoclinic (m) phase is not present in the AFE films. The largest diffraction peak near 40 ° originates from the W bottom contact.

By performing pixel-by-pixel BE-PFM on-field hysteresis measurements, we were able to identify quad-peaked amplitude versus electric field features that indicate the presence of piezoelectric signatures of AFE in both ZrO_2-based films (Figure S1, Supporting Information). Further comparisons of the off-field and on-field piezoresponse with FE La-doped HfO_2 and AlScN can be found in the Supporting Information. The mean piezoelectric response shows that Hf-doping of ZrO_2 enhances piezoelectricity as seen in **Figure 4**. The enhancement in ZrO_2 piezoelectricity

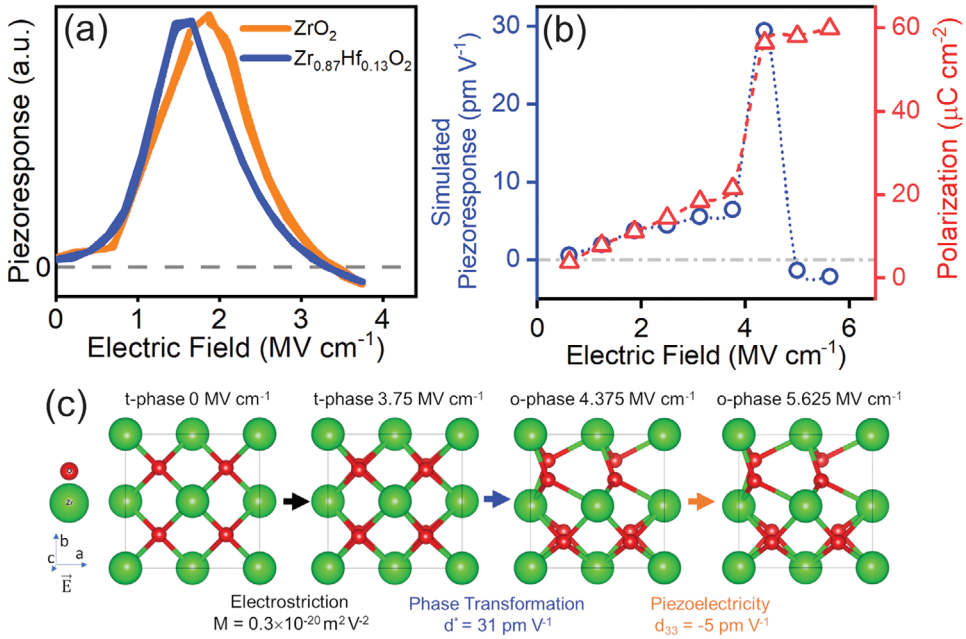

Figure 5. Piezoelectric response measured by BE-PFM and calculated by molecular dynamics. a) Experimental unipolar piezoresponse versus electric field measured on ZrO_2 and $Zr_{0.87}Hf_{0.13}O_2$ by BE-PFM. b) Simulated piezoresponse and polarization versus electric field produced from molecular dynamic simulations of the electric-field driven tetragonal to polar orthorhombic phase transition. c) Molecular dynamic simulations showing the change in lattice with an electric field-induced phase transition from the nonpolar tetragonal to the polar orthorhombic phase. The inversion of the sign of the piezoresponse is consistent with the sign inversion of the simulated d_{33} from the polar orthorhombic phase. The overestimation of the simulated phase transition field is a result of the density functional used.

is expected from the increased magnitude of switched charge and closer proximity to the morphotropic phase boundary with Hf-doping.

The enhanced amplitude of the piezoresponse agrees with the larger switched polarization charge observed in the polarization-electric field double hysteresis loops. The asymmetry found with electric field polarity manifests again at the microscopic scale in the piezoelectric response, where the larger magnitude of switched charge associated with the positive field-induced phase transition leads to a larger amplitude and piezoresponse as seen in Figure 4a,c, further confirming the piezoelectric dependence on the switched charge. As shown in Figure 4b, the phase is 0° up to applied field strengths of 2 – 2.5 MV cm^{-1} then jumps to 180° in both films at higher strengths above the phase transition field. The converse phase response is observed with negative applied electric fields. Phase calibration was performed with reference to AlScN and La-doped HfO_2 films, which are shown to have opposite signs of the piezoelectric coefficient, d_{eff} (see Supporting Information).[46]

Figure 5a shows unipolar BE-PFM hysteresis measurements on the ZrO_2-based films. A significant peak in piezoresponse is observed that decreases and eventually reverses sign at higher electric fields, which is in agreement with the phase jump observed at high fields during the bipolar BE-PFM hysteresis measurements. Molecular dynamics (MD) simulations were performed to calculate the piezoresponse-electric field characteristics of ZrO_2 caused by the evolution of the electric field induced tetragonal to polar orthorhombic phase transition. Figure 5b shows the MD simulated piezoresponse where distinct behavior in three electric field ranges is observed. At low fields, the simulated piezoresponse originates from electrostriction of the t-phase, which is low in magnitude and positive. The magnitude of the piezoresponse increases by a factor of roughly 5 at the tetragonal to polar orthorhombic field-induced phase transition due to the volume expansion of the lattice cell, as depicted in Figure 5c. Simulations show that as the electric field is increased beyond the phase transition, the d_{33} originates from the inverse piezoelectric effect of the polar orthorhombic phase, which has roughly the same magnitude as the electrostriction effect of the t-phase but is negative in sign.

From the atomistic modelling perspective, the PFM data offer an unexpected opportunity to validate the quantum mechanical models describing the kinetic barrier for solid-state phase transformations which are related to the electric field needed for the phase transition. It turns out that the used PBEsol density functional, which has been optimized for excellent lattice size, overestimates the kinetic barrier by about a factor of two (as shown in Figure S2, Supporting Information). Despite the overestimation of the kinetic barrier from the adopted density functional, there is excellent agreement between the experimentally observed and simulated piezoresponse as a result of an electric field induced tetragonal to polar orthorhombic phase transition, thus confirming the physical mechanism responsible for AFE behavior in ZrO_2-based films.

4. Imaging Electric Field Induced Phase Transitions at the Nanoscale

Antiferroelectrics are generally difficult to experimentally probe because structural relaxations occur once the applied electric field

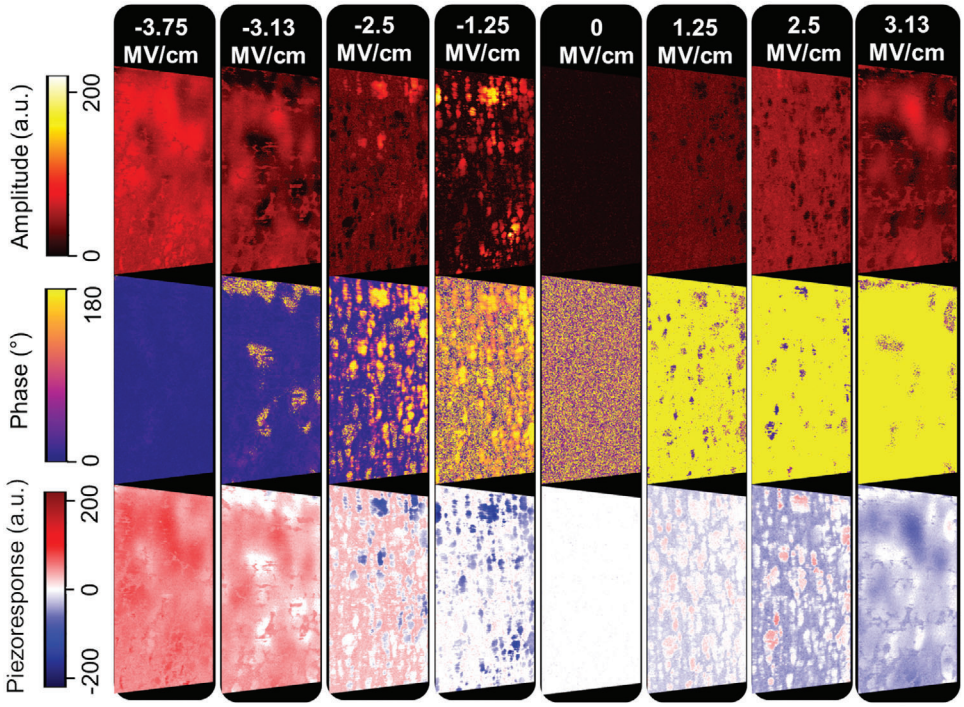

Figure 6. BE-PFM images of 350 nm × 350 nm of ZrO_2 with DC electric field biases to provide a snapshot-by-snapshot evolution of the electric field-induced phase transitions. Without a DC electric field, ZrO_2 is not piezoelectric.

is removed. In Figure 2 and as reported elsewhere, no discernable piezoelectric features are present in a zero-DC field PFM scan of AFE ZrO_2.[22] To overcome this limitation, BE-PFM imaging was performed with the bottom electrode grounded and with a DC electric field offset through the conducting PFM cantilever tip as it is scanned across the surface of the ZrO_2-based capacitors. By modifying BE-PFM imaging with a DC field, features of electric field-induced phase transitions that were previously invisible now become apparent, as shown in **Figure 6**.

In contrast to FEs that exhibit a well-defined piezoresponse from the retained polarization state, AFEs lose their polar state when the electric field is removed. As the DC electric fields are lowered below the phase transition fields, and then are removed completely, BE-PFM imaging shows the amplitude and piezoresponse approach zero due to the loss of the polar state in ZrO_2, as seen in the 350 nm × 350 nm BE-PFM images in Figure 6. However, when DC fields near the phase transition fields are applied, granular regions on the order of 3-20 nm show significant amplitude, phase, and piezoresponse contrast compared to surrounding regions because of the phase transition to a polar state. The red-blue contrast in the piezoresponse across the film surface shows that the electromechanical response of the film is not uniform and that the phase transitions are highly localized. The nanoscale regions undergoing phase transitions first displace in one direction during the phase transition, then reverse sign as the electric field is increased beyond the phase transition field, which is in excellent agreement with molecular dynamic simulations and PFM hysteresis spectroscopy.

Using the same experimental approach, BE-PFM imaging was again performed but this time on $Zr_{0.87}Hf_{0.13}O_2$ with a 100 nm × 100 nm area to obtain higher resolution of the nanoscale electric field-induced phase transitions, as shown in **Figure 7**. When a −1.88 MV cm^{-1} DC electric field is applied through the cantilever tip, the negative electric field-induced phase transition becomes pronounced with a 180° phase and contraction of the film surface. This observation is in complete agreement with the series of images of the phase transition on top of the undoped ZrO_2 surface. The positive electric field-induced phase transitions are more clearly visible in the 100 nm × 100 nm images, with the red-colored piezoresponse of single grains undergoing phase transitions gradually weakening and inverting in sign as the DC electric field is increased.

A closer inspection of the 350 nm × 350 nm BE-PFM images of ZrO_2 near the field-induced phase transition at −1.25 MV cm^{-1} is provided in **Figure 8**. The nanometer-sized grains undergoing phase transitions show extraordinary amplitude contrast compared to regions that appear electrostrictive, as shown in Figure 8a. A phase transition at −1.25 MV cm^{-1} DC field induces a 180° phase transition, whereas the phase of the rest of the film is poorly defined and noisy, as shown in Figure 8c. The piezoresponse image shows the film contracting when the AC field through the cantilever acts against the DC field polarity that "freezes" the phase transition in place, in contrast to surrounding regions that appear to show a weak piezoresponse, as seen in Figure 8e.

4.1. Results and Discussion

Upon closer inspection of the higher resolution 100 nm × 100 nm BE-PFM images, regions undergoing phase transitions in Hf-doped ZrO_2 exhibit a strong amplitude and a 180° phase

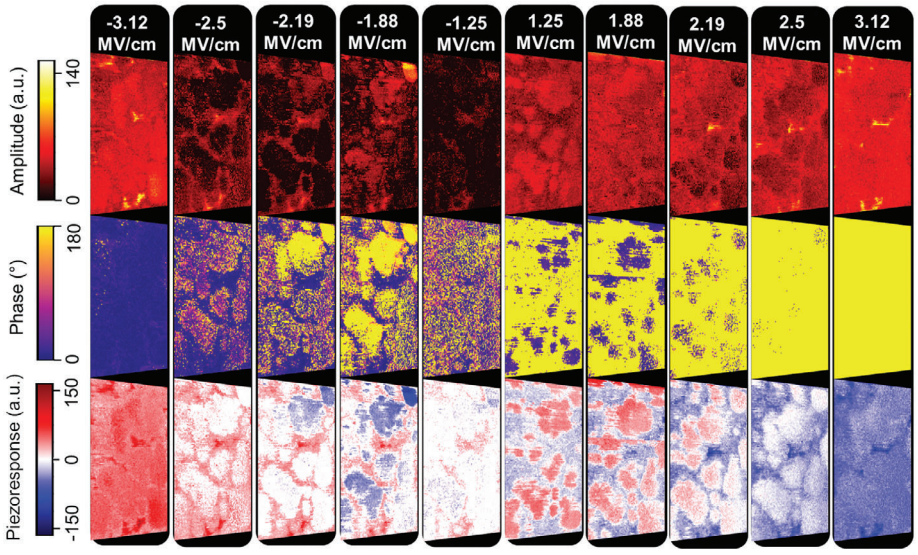

Figure 7. BE-PFM images of 100 nm × 100 nm of Hf-doped ZrO_2 with DC electric field biases. Phase transitions occur in regions that show a sign change in phase and piezoresponse as the electric field magnitude is increased.

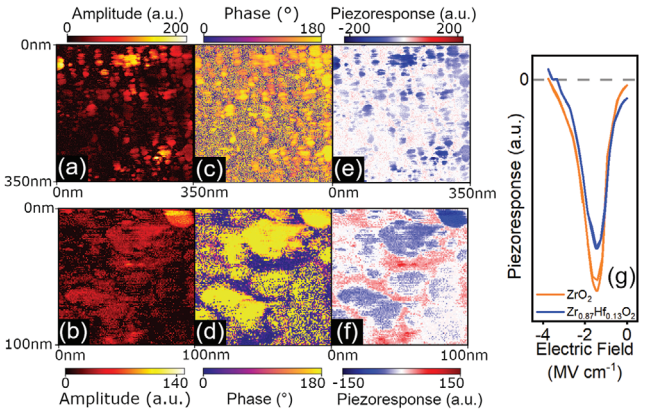

Figure 8. BE-PFM images capturing phase transitions in ZrO_2-based films near the phase transition fields. 350 nm × 350 nm BE-PFM a) amplitude, c) phase, and e) piezoresponse images of ZrO_2 under a −1.25 MV cm^{-1} DC field. 100 nm × 100 nm BE-PFM b) amplitude, d) phase, and f) piezoresponse images of $Zr_{0.87}Hf_{0.13}O_2$ under a −1.88 MV cm^{-1} DC field. g) Piezoresponse versus electric field measured locally with BE-PFM hysteresis. The DC fields applied during imaging are near the peak piezoresponse of the phase transition.

(Figure 8b,d). Regions that show phase transitions exhibit contraction of the film surface (Figure 8f). Small crystallites can impede the ability to induce a phase transition by increasing the phase transition field (Supporting Information). To confirm that the BE-PFM images reflect the true nature of the AFE electromechanical response of ZrO_2, negative unipolar measurements of the piezoresponse were obtained independently from BE-PFM hysteresis spectroscopy as shown in Figure 8g. The piezoresponse sign and magnitude from hysteresis are in agreement with the sign and magnitudes found in the phase transitions during imaging, providing unequivocal evidence that the BE-PFM images accurately capture the AFE behavior of the capacitor surface. Therefore, these BE-PFM images under varying DC fields provide a clear snapshot of all the features of the phase transition obtained during hysteresis spectroscopy on the capacitor surface.

5. Conclusion

Nanoscale phase transitions in AFE ZrO_2 have been imaged for the first time by BE-PFM, providing undeniable evidence that reversible electric field-induced phase transitions are responsible for the unique nonlinear dielectric behavior in ZrO_2-based AFE films. Molecular dynamics simulations demonstrated the characteristic electromechanical response of electric field-induced phase transitions in ZrO_2 that arise from the progressive evolution of i) the electrostrictive effect from the tetragonal phase, ii) the lattice cell volume expansion generated from the tetragonal to orthorhombic phase transition, and then iii) the piezoelectric response of the polar orthorhombic phase as the magnitude of the electric field was increased beyond the transition field. Each characteristic change in piezoresponse found by simulation was in remarkable agreement to the piezoresponse probed experimentally by BE-PFM.

The agreement of two independent measurements in BE-PFM, hysteresis spectroscopy and imaging under DC fields, further confirmed the authentic nature of the reversible field induced phase transitions responsible for AFE behavior in ZrO_2-based films. BE-PFM was also used to unambiguously distinguish pinched La-doped HfO_2 from AFE ZrO_2, clearly illustrating that FE domains are not responsible for the double P-E hysteresis loop. The discovery of independent and reversible phase transitions in nanometer-sized grains under applied electric fields opens up new possibilities for nanoelectronic devices.

6. Experimental Section

Capacitor Fabrication: Thin film capacitors consisting of a W/TiN/$Zr_{1-x}Hf_xO_2$/TiN/Ti/Pt stack were deposited on (100) Si wafers. An

ultra-high vacuum Bestec cluster physical vapor deposition tool (PVD) was used to sputter W and TiN. Approximately 30 nm of W was sputter deposited on the Si substrate at room temperature. The W layer serves as a low resistance contact to the bottom electrode. An ≈12 nm TiN layer was sputtered on top of the W layer at room temperature. An Oxford Instruments atomic layer deposition (ALD) tool was used to grow 8 nm thick $Zr_{1-x}Hf_xO_2$ at 280 °. The precursors used for Zr and Hf were ZyALD ($CpZr[N(CH_3)_2]_3$) and HyALD ($CpHf[N(CH_3)_2]_3$, respectively. A Zr:Hf cycling ratio of 8:1 was used to grow $Zr_{0.87}Hf_{0.13}O_2$. An ≈12 nm TiN layer was sputtered on top of the $Zr_{1-x}Hf_xO_2$ films to form the top electrode at room temperature. The blanket ZrO_2 metal-insulator-metal capacitor structure was then annealed at 500 °C for 20 s in N_2. The ≈13 nm La-doped HfO_2 films were processed with a 10:1 Hf:La ratio with further processing conditions described elsewhere.[30]

Lithography was performed using a Heidelberg Instruments μPG 101 laser lithography patterning tool. Ti (5 nm) and Pt (10 nm) were deposited using an evaporator from Bestec GmbH. Pt was deposited to act as hard mask during the inductively coupled plasma (ICP) etching process. The top contacts were defined by lift-off in acetone followed by ICP etching to remove the TiN in between the Ti/Pt top contacts. The etching step was performed at room temperature using a Plasmalab System133 from Oxford Instruments with an RF power of 120 W and an ICP power of 1200 W at 10 mTorr. The ICP etch chemistry was a 3:2:1 ratio of SF_6:O_2:Ar. A variety of capacitors areas ranging from 10000 – 25 μm^2 were available for electrical probing. Band-excitation piezoresponse force microscopy (BE-PFM) was performed on the smallest capacitors.

Physical and Electrical Characterization: A Bruker D8 Discover was used to perform x-ray reflectivity (XRR) and grazing incidence x-ray diffraction (GIXRD) to determine the thickness and crystalline structure of the ZrO_2-based thin films respectively. Both ZrO_2-based films were determined to be ≈8 nm thick. Dynamic hysteresis measurements were performed on an Aixacct ferroelectric measurement instrument to acquire polarization versus electric field (P-E) and current density versus electric field (J-E) at a measurement frequency of 1 kHz. All dynamic hysteresis measurements were performed on pristine devices without cycling.

In this study, a commercial Cypher AFM (Asylum Research an Oxford Instruments company, Santa Barbara, CA) was used to conduct PFM measurements with Pt-coated cantilevers (ElectriMulti75-G, Budget Sensors) having a nominal spring constant of ≈3 N m^{-1} and a resonance frequency of ≈75 kHz. BE-PFM was performed with external data acquisition electronics based on a NI-6115 fast DAQ card controlled by custom-built Labview software. BE-PFM measurements were performed on the top electrode surface of ZrO_2-based capacitors as shown in Figure S3 (Supporting Information). The BE-PFM experimental data was saved in h5 files and processed using the python pycroscopy package. BE-PFM measurements were performed on pristine capacitors that did not receive any pre-poling.

Molecular Dynamics Description: The molecular dynamics simulations were conducted using the Large-scale Atomic/Molecular Massively Parallel Simulator (LAMMPS). The utilized interatomic force potential was machine learned using the DeepMD-Kit [47] based on the Perdew-Burke-Ernzerhof revised for solids (PBEsol) potential and is described in detail in.[48] By stacking one monolayer of tetragonal (t) phase with 5 × 5 × 1 12 atomic unit cells surface on top of ferroelectric polar orthorhombic (o) phase with a size of 5 × 5 × N (N = 6–12) 12 atomic unit cells, with the o-phase being polarized in direction of the t-phase, varying surface to volume ratios can be generated. To prevent the decay of the smaller t-phase portion into the "bulk" o-phase, the oxygen atoms were fixed, parallel to the polarization direction of the o-phase, using the fix spring/atom command from LAMMPS. Simulating a 3,5 nm thick layer of ZrO_2 results in a Curie-temperature of below 100 K and AFE behavior at room temperature, at which simulations of the evolution of the phase structure under electric fields were performed, as seen in Figure S7 (Supporting Information). The interfacial t-phase was constrained as a way to force the ground state of the rest of the ZrO_2 crystallite into the t-phase through the depolarization effect at zero field,[49] thus allowing MD to identify if phase transitions would proceed in the presence of an electric field. This method results in stress in the oxygen sublattice leading to a reduction of the Curie-temperature from ≈600–700K, from free energies calculations for "bulk"-phases, to below room temperature for a fixed oxygen sublattice in the monolayer. By assigning Born-charges to the atoms, derived from Berry-phase calculations (Zr = 5.10e, O = −2.55e), a homogeneous external electric field could be applied to the material during the simulations which introduces an error from the charges changing during the transformation on the order of 10%. To improve the model for the description of thermal expansion,[48] a quantum thermal bath model was added. The simulations were carried out using an anisotropic Nose-Hoover style NPT ensemble as implemented in the LAMMPS code. The time-step was chosen to be 1 fs, the thermostat damping parameter 400 fs, the barostat damping parameter to be 10 ps with a drag factor of 2, the transient times were 3 ps for calculations below the phase-transition temperature and 8 ps above the phase-transition temperature to allow the simulation to reach equilibrium after the phase-transition. The final results were obtained after averaging 40 ps. The raw data from the molecular dynamics simulation are time-averaged can be seen in Figure S8 (Supporting Information).

Supporting Information

Supporting Information is available from the Wiley Online Library or from the author.

Acknowledgements

The authors would like to acknowledge Sabine Neumayer and Pratyush Buragohain for helpful discussions on piezoresponse force microscopy. P.L., B.X., and R.G. were funded by the German Research Foundation (DFG)—Project No. 430054035 and 433647091. R.G. was funded by the German Research Foundation (DFG)—Project No. 458372836. This work was financially supported out of the state budget approved by the delegates of the Saxon State Parliament. Piezoresponse force microscopy measurements were supported by the Center for Nanophase Materials Sciences (CNMS), which is a US Department of Energy (DOE), Office of Science User Facility at Oak Ridge National Laboratory. The United States Government retains and the publisher, by accepting the article for publication, acknowledges that the United States Government retains a nonexclusive, paid-up, irrevocable, worldwide license to publish or reproduce the published form of this manuscript, or allow others to do so, for the United States Government purposes. The Department of Energy will provide public access to these results of federally sponsored research in accordance with the DOE Public Access Plan (https://www.energy.gov/downloads/doe-public-access-plan).

Open access funding enabled and organized by Projekt DEAL.

Conflict of Interest

The authors declare no conflict of interest.

Data Availability Statement

The data that support the findings of this study are available from the corresponding author upon reasonable request.

Keywords

antiferroelectrics, phase transitions, piezoelectrics, piezoresponse force microscopy, zirconia

Received: April 1, 2023
Revised: May 17, 2023
Published online:

[1] L. M. Krauss, S. Dodelson, S. Meyer, *Science* **2010**, *328*, 989.

[2] D. Boyanovsky, H. J. de Vega, D. J. Schwarz, *Annu. Rev. Nucl. Part. Sci.* **2006**, *56*, 441.
[3] Y. Aoki, G. Endrődi, Z. Fodor, S. D. Katz, K. K. Szabó, *Nature* **2006**, *443*, 675.
[4] S. S. Cheema, N. Shanker, L.-C. Wang, C.-H. Hsu, S.-L. Hsu, Y.-H. Liao, M. San Jose, J. Gomez, W. Chakraborty, W. Li, J.-H. Bae, S. K. Volkman, D. Kwon, Y. Rho, G. Pinelli, R. Rastogi, D. Pipitone, C. Stull, M. Cook, B. Tyrrell, V. A. Stoica, Z. Zhang, J. W. Freeland, C. J. Tassone, A. Mehta, G. Saheli, D. Thompson, D. I. Suh, W.-T. Koo, K.-J. Nam, et al., *Nature* **2022**, *604*, 65.
[5] S. Datta, W. Chakraborty, M. Radosavljevic, *Science* **2022**, *378*, 733.
[6] T. Mikolajick, S. Slesazeck, H. Mulaosmanovic, M. H. Park, S. Fichtner, P. D. Lomenzo, M. Hoffmann, U. Schroeder, *J. Appl. Phys.* **2021**, *129*, 100901.
[7] M. Ghatge, G. Walters, T. Nishida, R. Tabrizian, *Nat. Electron.* **2019**, *2*, 506.
[8] F. Ali, D. Zhou, M. Ali, H. W. Ali, M. Daaim, S. Khan, M. M. Hussain, N. Sun, *ACS Appl. Electron. Mater.* **2020**, *2*, 2301.
[9] S. Lee, Y. Lee, T. Kim, G. Kim, T. Eom, H. Shin, Y. Jeong, S. Jeon, *ACS Appl. Mater. Interfaces* **2022**, *14*, 53019.
[10] S. E. Kim, J. Y. Sung, J. D. Jeon, S. Y. Jang, H. M. Lee, S. M. Moon, J. G. Kang, H. J. Lim, H.-S. Jung, S. W. Lee, *Adv. Mater. Technol.* **2022**, 2200878.
[11] Y. He, G. Zheng, X. Wu, W.-J. Liu, D. W. Zhang, S.-J. Ding, *Nanoscale Adv.* **2022**, *4*, 4648.
[12] G. H. Park, D. H. Lee, H. Choi, T. Kwon, Y. H. Cho, S. H. Kim, M. H. Park, *ACS Appl. Electron. Mater.* **2023**, *5*, 642.
[13] R. Cao, X. Zhang, S. Liu, J. Lu, Y. Wang, H. Jiang, Y. Yang, Y. Sun, W. Wei, J. Wang, H. Xu, Q. Li, Q. Liu, *Nat. Commun.* **2022**, *13*, 7018.
[14] T. D. Huan, V. Sharma, G. A. Rossetti, R. Ramprasad, *Phys. Rev. B* **2014**, *90*, 064111.
[15] R. Materlik, C. Künneth, A. Kersch, *J. Appl. Phys.* **2015**, *117*, 134109.
[16] S. E. Reyes-Lillo, K. F. Garrity, K. M. Rabe, *Phys. Rev. B* **2014**, *90*, 140103.
[17] M. H. Park, C. S. Hwang, *Rep. Prog. Phys.* **2019**, *82*, 124502.
[18] P. D. Lomenzo, U. Schroeder, T. Mikolajick, presented at 2021 IEEE Int. Symp. on Applications of Ferroelectrics (ISAF), Sydney, Australia, May **2021**.
[19] P. D. Lomenzo, S. Slesazeck, T. Mikolajick, U. Schroeder, presented at 2020 IEEE Int. Memory Workshop (IMW), Dresden, Germany, May **2020**.
[20] M. Pešić, M. Hoffmann, C. Richter, T. Mikolajick, U. Schroeder, *Adv. Funct. Mater.* **2016**, *26*, 7486.
[21] S. Starschich, U. Böttger, *J. Appl. Phys.* **2018**, *123*, 044101.
[22] P. D. Lomenzo, M. Materano, T. Mittmann, P. Buragohain, A. Gruverman, T. Kiguchi, T. Mikolajick, U. Schroeder, *Adv. Electron. Mater.* **2022**, *8*, 2100556.
[23] J. Müller, T. S. Böscke, U. Schröder, S. Mueller, D. Bräuhaus, U. Böttger, L. Frey, T. Mikolajick, *Nano Lett.* **2012**, *12*, 4318.
[24] X. Luo, K. Toprasertpong, M. Takenaka, S. Takagi, *Appl. Phys. Lett.* **2021**, *118*, 232904.
[25] S.-H. Yi, B.-T. Lin, T.-Y. Hsu, J. Shieh, M.-J. Chen, *J. Eur. Ceram. Soc.* **2019**, *39*, 4038.
[26] T. Mimura, T. Shimizu, O. Sakata, H. Funakubo, *Appl. Phys. Lett.* **2021**, *118*, 112903.
[27] U. Schroeder, T. Mittmann, M. Materano, P. D. Lomenzo, P. Edgington, Y. H. Lee, M. Alotaibi, A. R. West, T. Mikolajick, A. Kersch, J. L. Jones, *Adv. Electron. Mater.* **2022**, *8*, 2200265.
[28] M. H. Lee, Y.-T. Wei, K.-Y. Chu, J.-J. Huang, C.-W. Chen, C.-C. Cheng, M.-J. Chen, H.-Y. Lee, Y.-S. Chen, L.-H. Lee, M.-J. Tsai, *IEEE Electron Device Lett.* **2015**, *36*, 294.
[29] S. Jesse, S. V. Kalinin, R. Proksch, A. P. Baddorf, B. J. Rodriguez, *Nanotechnology* **2007**, *18*, 435503.
[30] U. Schroeder, C. Richter, M. H. Park, T. Schenk, M. Pešić, M. Hoffmann, F. P. G. Fengler, D. Pohl, B. Rellinghaus, C. Zhou, C.-C. Chung, J. L. Jones, T. Mikolajick, *Inorg. Chem.* **2018**, *57*, 2752.
[31] C. Mart, K. Kühnel, T. Kämpfe, S. Zybell, W. Weinreich, *Appl. Phys. Lett.* **2019**, *114*, 102903.
[32] T. Schenk, E. Yurchuk, S. Mueller, U. Schroeder, S. Starschich, U. Böttger, T. Mikolajick, *Appl. Phys. Rev.* **2014**, *1*, 041103.
[33] A. M. Walke, M. I. Popovici, K. Banerjee, S. Clima, P. Kumbhare, J. Desmet, J. Meersschaut, G. V. den Bosch, R. Delhougne, G. S. Kar, J. V. Houdt, *IEEE Trans. Electron Devices* **2022**, *69*, 4744.
[34] M. Lederer, K. Mertens, R. Olivo, K. Kühnel, D. Lehninger, T. Ali, T. Kämpfe, K. Seidel, L. M. Eng, *J. Mater. Res.* **2021**, *36*, 4370.
[35] S. Kirbach, M. Lederer, S. Eßlinger, C. Mart, M. Czernohorsky, W. Weinreich, T. Wallmersperger, *Appl. Phys. Lett.* **2021**, *118*, 012904.
[36] P. D. Lomenzo, C. Richter, M. Materano, T. Mikolajick, U. Schroeder, T. Schenk, D. Spirito, S. Gorfman, presented at 2020 Joint Conf. of the IEEE Int. Frequency Control Symp. and Int. Symp. on Applications of Ferroelectrics (IFCS-ISAF) Keystone, Co, USA, July **2020**.
[37] S. Lombardo, C. Nelson, K. Chae, S. Reyes-Lillo, M. Tian, N. Tasneem, Z. Wang, M. Hoffmann, D. Triyoso, S. Consiglio, K. Tapily, R. Clark, G. Leusink, K. Cho, A. Kummel, J. Kacher, A. Khan, presented at 2020 IEEE Symp. on VLSI Technology, Honolulu, HI, USA, June **2020**.
[38] S. S. Fields, S. W. Smith, P. J. Ryan, S. T. Jaszewski, I. A. Brummel, A. Salanova, G. Esteves, S. L. Wolfley, M. D. Henry, P. S. Davids, J. F. Ihlefeld, *ACS Appl. Mater. Interfaces* **2020**, *12*, 26577.
[39] P. D. Lomenzo, C. Richter, T. Mikolajick, U. Schroeder, *ACS Appl. Electron. Mater.* **2020**, *2*, 1583.
[40] S. Jesse, S. V. Kalinin, *J. Phys. D: Appl. Phys.* **2011**, *44*, 464006.
[41] M. Kohli, P. Muralt, N. Setter, *Appl. Phys. Lett.* **1998**, *72*, 3217.
[42] D. Zhou, J. Xu, Q. Li, Y. Guan, F. Cao, X. Dong, J. Müller, T. Schenk, U. Schröder, *Appl. Phys. Lett.* **2013**, *103*, 192904.
[43] Z. Wang, A. A. Gaskell, M. Dopita, D. Kriegner, N. Tasneem, J. Mack, N. Mukherjee, Z. Karim, A. I. Khan, *Appl. Phys. Lett.* **2018**, *112*, 222902.
[44] W. Hamouda, A. Pancotti, C. Lubin, L. Tortech, C. Richter, T. Mikolajick, U. Schroeder, N. Barrett, *J. Appl. Phys.* **2020**, *127*, 064105.
[45] M. Hyuk Park, H. Joon Kim, Y. Jin Kim, W. Lee, T. Moon, C. Seong Hwang, *Appl. Phys. Lett.* **2013**, *102*, 242905.
[46] P. Buragohain, H. Lu, C. Richter, T. Schenk, P. Kariuki, S. Glinsek, H. Funakubo, J. Íñiguez, E. Defay, U. Schroeder, A. Gruverman, *Adv. Mater.* **2022**, *34*, 2206237.
[47] L. Zhang, J. Han, H. Wang, R. Car, E. Weinan, *Phys. Rev. Lett.* **2018**, *120*, 143001.
[48] R. Ganser, S. Bongarz, A. von Mach, L. Azevedo Antunes, A. Kersch, *Phys. Rev. Appl.* **2022**, *18*, 054066.
[49] C. Künneth, R. Materlik, A. Kersch, *J. Appl. Phys.* **2017**, *121*, 205304.
[50] A. Gruverman, M. Alexe, D. Meier, *Nat. Commun.* **2019**, *10*, 1661.
[51] L. Collins, Y. Liu, O. S. Ovchinnikova, R. Proksch, *ACS Nano* **2019**, *13*, 8055.
[52] S. M. Neumayer, S. Saremi, L. W. Martin, L. Collins, A. Tselev, S. Jesse, S. V. Kalinin, N. Balke, *J. Appl. Phys.* **2020**, *128*, 171105.
[53] S. M. Neumayer, E. A. Eliseev, M. A. Susner, A. Tselev, B. J. Rodriguez, J. A. Brehm, S. T. Pantelides, G. Panchapakesan, S. Jesse, S. V. Kalinin, M. A. McGuire, A. N. Morozovska, P. Maksymovych, N. Balke, *Phys. Rev. Mater.* **2019**, *3*, 024401.
[54] S. Dutta, P. Buragohain, S. Glinsek, C. Richter, H. Aramberri, H. Lu, U. Schroeder, E. Defay, A. Gruverman, J. Íñiguez, *Nat. Commun.* **2021**, *12*, 7301.

[55] M. Falkowski, A. Kersch, *Appl. Phys. Lett.* **2021**, *118*, 032905.
[56] M. Hoffmann, U. Schroeder, C. Künneth, A. Kersch, S. Starschich, U. Böttger, T. Mikolajick, *Nano Energy* **2015**, *18*, 154.
[57] P. Buragohain, A. Erickson, P. Kariuki, T. Mittmann, C. Richter, P. D. Lomenzo, H. Lu, T. Schenk, T. Mikolajick, U. Schroeder, A. Gruverman, *ACS Appl. Mater. Interfaces* **2019**, *11*, 35115.